

Research Paper

Injectable and in situ crosslinkable gelatin microribbon hydrogels for stem cell delivery and bone regeneration *in vivo*

Yaohui Tang¹, Xinming Tong¹, Bogdan Conrad², Fan Yang^{1,3}✉

1. Department of Orthopaedic Surgery, Stanford University School of Medicine, Stanford, CA, 94305, USA.
2. Program of Stem Cell Biology and Regenerative Medicine, Stanford University School of Medicine, 300 Pasteur Dr., Edwards R105, Stanford, CA, 94305, USA.
3. Department of Orthopaedic Surgery, Stanford University School of Medicine, 300 Pasteur Dr., Edwards R105, Stanford, CA, 94305, USA.

✉ Corresponding author: Prof. Fan Yang, Ph.D., Associate Professor, Departments of Orthopaedic Surgery and Bioengineering, Director of Stem Cells and Biomaterials Engineering Laboratory, Stanford University School of Medicine, 300 Pasteur Dr., Edwards R105, Stanford, CA 94305, USA. E-mail: fanyang@stanford.edu; Phone: (650) 725-7128; Fax: (650) 723-9730

© The author(s). This is an open access article distributed under the terms of the Creative Commons Attribution License (<https://creativecommons.org/licenses/by/4.0/>). See <http://ivyspring.com/terms> for full terms and conditions.

Received: 2019.10.11; Accepted: 2020.04.27; Published: 2020.05.15

Abstract

Rationale: Injectable matrices are highly desirable for stem cell delivery. Previous research has highlighted the benefit of scaffold macroporosity in enhancing stem cell survival and bone regeneration *in vivo*. However, there remains a lack of injectable and in situ crosslinkable macroporous matrices for stem cell delivery to achieve fast bone regeneration in immunocompetent animal model. The goal of this study is to develop an injectable gelatin-based μ RB hydrogel supporting direct cell encapsulation that is available in clinics as macroporous matrices to enhance adipose-derived stromal cell (ASC) survival, engraftment and accelerate bone formation in craniofacial defect mouse.

Methods: Injectable and in situ crosslinkable gelatin microribbon (μ RB)-based macroporous hydrogels were developed by wet-spinning. Injectability was optimized by varying concentration of glutaraldehyde for intracrosslinking of μ RB shape, and fibrinogen coating. The efficacy of injectable μ RBs to support ASCs delivery and bone regeneration were further assessed *in vivo* using an immunocompetent mouse cranial defect model. ASCs survival was evaluated by bioluminescent imaging and bone regeneration was assessed by micro-CT. The degradation and biocompatibility were determined by histological analysis.

Results: We first optimized injectability by varying concentration of glutaraldehyde used to fix gelatin μ RBs. The injectable μ RB formulation were subsequently coated with fibrinogen, which allows in situ crosslinking by thrombin. Fluorescence imaging and histology showed majority of μ RBs degraded by the end of 3 weeks. Injectable μ RBs supported comparable level of ASC proliferation and bone regeneration as implantable prefabricated μ RB controls. Adding low dosage of BMP2 (100 ng per scaffold) with ASCs substantially accelerated the speed of mineralized bone regeneration, with 90% of the bone defect refilled by week 8. Immunostaining showed M1 (pro-inflammatory) macrophages were recruited to the defect at day 3, and was replaced by M2 (anti-inflammatory) macrophages by week 2. Adding μ RBs or BMP2 did not alter macrophage response. Injectable μ RBs supported vascularization, and BMP-2 further enhanced vascularization.

Conclusions: Our results demonstrated that μ RB-based scaffolds enhanced ASC survival and accelerated bone regeneration after injection into critical sized cranial defect mouse. Such injectable μ RB-based scaffold can provide a versatile biomaterial for delivering various stem cell types and enhancing tissue regeneration.

Key words: bone, hydrogels, injectable, macroporous, stem cells

Introduction

Stem cell transplantation has shown great potential for tissue regeneration. However, delivering cells alone usually results in poor cell survival and

engraftment [1-3], and do not provide any structural support [4]. To enhance the therapeutic outcomes, biomaterials have been widely used as

three-dimensional artificial niche for cell delivery with tunable biochemical and physical cues [5-7]. Hydrogels are popular biomaterials for cell delivery due to injectability, ease of cell encapsulation, and tissue-like water content [8, 9]. However, hydrogels are crosslinked polymeric network, which typically contain mesh size orders of magnitude smaller than the size of cells [10]. To overcome such physical constraints, degradation may be introduced to support cell proliferation and new matrix deposition, but the ability of cells to degrade matrices vary and degradation takes time, often leading to undesirable delayed tissue regeneration [11].

In addition to degradation, macroporosity have also been introduced to scaffolds to help overcome physical constraint and accelerate the speed of vascularization and new tissue regeneration [12-14]. Conventional methods to introduce macroporosity include particle leaching [15], phase separation [16], gas foaming [17], micro-extrusion [18], electrospinning [19], and 3D printing [20]. However, these methods often involve steps that are not cell-friendly, and cells can only be seeded onto the prefabricated scaffolds. This results in undesirable heterogeneous cell distributions and do not support injectability and in situ polymerization.

Given the limitations of conventional macroporous scaffolds, injectable scaffolds have become more attractive due to the ease of handling and reduced invasiveness [21]. However, the injectable scaffolds with macroporosity are limited. Approaches have been exploited to fabricate injectable macroporous scaffolds for cell delivery [13, 22]. For example, macroporous cryo-hydrogels have been developed as cell carrier, which possess shape-memory properties that withstand reversible deformation and allow rapid volume recovery post injection [23-25]. These cryo-hydrogels have shown to support cell retention and survival post-injection in vivo. However, in order to allow homogenous cell infiltration and easier injection, these cryo-hydrogels can only be used with relatively small size, ranging from hundreds of micrometers to a few millimeters. In addition, these porous scaffolds are prefabricated, which could limit cell infiltration by the pore size and the loading method.

In contrast, the bottom-up approaches using injectable building blocks to build up macroporous scaffolds in situ are more facile and advantageous, due to the ensured interconnected macroporosity and homogeneous cell distribution. For example, injectable hydrogel microspheres can be annealed to form macroporous scaffolds [26, 27]. These microparticles were packed in high density to form a 3D scaffold, with pores formed by empty spaces

among the annealed spheres. The interconnected macroporosity substantially enhanced cell proliferation and helped integrating newly formed tissue with host tissue in the wound-healing model [26, 27]. However, this strategy requires high packing density to ensure contact between the microspheres, which could limit available porosity. The low ratios of surface area to volume may result in limited surface area to support cell seeding and growth. In addition, the relatively weak mechanical strength (10-1000 Pa) could limit its application for treating load-bearing tissues [26].

Compared to microspheres, building blocks with the geometry of fibers and ribbons can facilitate the inter-connection and provide higher surface area and porosity. For example, our lab has recently reported the development of a gelatin-based scaffold using microribbon (μ RB)-shaped hydrogels as building blocks that combines injectability and macroporosity [28]. The μ RB-based scaffold allows direct cell encapsulation in macroporous niche with homogenous cell distribution and robust proliferation [28]. In addition, the μ RBs has high diameter-to-length aspect ratio and high inter-connectivity in the scaffolds. These features render the μ RB scaffolds unique high mechanical flexibility and resilience, which can recover the original shape after 90% cyclic-strain compression [28, 29]. This makes it appropriate for engineering load-bearing tissues such as bone and cartilage. Delivering adipose-derived stromal cells (ASCs) using the μ RB-based macroporous scaffolds resulted in significantly increased cell survival in vivo and enhanced bone healing as compared to conventional nanoporous hydrogels [30].

While our previous work showed the potential of gelatin μ RBs as macroporous matrices for enhancing stem cell survival in vivo, several key bottlenecks remain before the translational potential of gelatin μ RBs for cell delivery can be fully realized. First, our previous gelatin μ RBs were prefabricated in vitro and not yet optimized for injection. Previous studies have shown cell viability are often compromised during injection due to increased shear forces, and specific optimization of the μ RB properties must be performed to identify optimized μ RB formulation that supports high cell viability after injection. Second, our previous gelatin μ RBs require light for polymerization, which are not suitable for polymerization in deep tissues with poor light penetration. Third, the speed of mineralized bone formation using gelatin μ RBs and ASCs remain slow and unsatisfactory, and degradation and biocompatibility of gelatin μ RBs in vivo remains largely unknown. To overcome these limitations, the

goal of this study is to develop injectable gelatin-based μ RBs that can form macroporous scaffolds in situ to support stem cell survival and bone regeneration in an immunocompetent mouse cranial defect model. We first assessed the degradation and inflammatory responses of optimized injectable gelatin-based μ RB scaffolds in vivo. We further exploited the potential of using the μ RBs to deliver BMP-2 and examined the synergy of BMP-2 with ASCs to promote bone regeneration.

Materials and Methods

Fabrication of gelatin-based microribbons (μ RBs)

Gelatin-based μ RBs were fabricated by wet-spinning as we previously reported [28]. Briefly, type-A gelatin (Sigma, USA) was dissolved in dimethyl sulfoxide (17% wt/wt) at 60 °C overnight, and ejected at 5 ml/h at room temperature into ethanol bath with constant stirring. The collected microfibers were transferred into acetone, with solvent exchange causing asymmetrical collapse of the microfibers into the microribbon (μ RB) shape. To lock the μ RB shape, the gelatin μ RBs were first intra-crosslinked in glutaraldehyde (GTA) solution under stirring overnight, neutralized for 2 h in L-lysine hydrochloride (1%) to block unreacted aldehyde groups, and washed at least six times with deionized water. To allow inter-crosslinking among gelatin μ RBs later for cell encapsulation, fixed μ RBs were suspended in fibrinogen (FB) solution (0.1% or 0.5%) overnight, and then washed eight times with deionized water. The μ RB products were then freeze-dried and stored at -20°C before use. For in vivo tracking of degradation of μ RBs, gelatin μ RBs were labeled with Alexa Fluor-700 or rhodamine. Specifically, 1 mg of Alexa Fluor 700 NHS Ester (Thermo Scientific, Barrington, IL, USA) or rhodamine NHS Ester (Thermo Scientific) was added into 200 ml glutaraldehyde solution for labeling 1 g μ RBs.

Characterizing the stiffness of μ RBs using atomic force microscopy

The stiffness of individual gelatin μ RB is tuned by varying concentration of glutaraldehyde (12.5%, 20% and 37.5%), which controls the degree of polymerization between amine groups within gelatin and glutaraldehyde. The stiffness of the μ RBs was measured in PBS at 37°C using a NX-10 atomic force microscope (Park System), equipped with a probe with silicon nitride cantilever with 2 μ m colloidal tip (NanoAndMore). A non-contact mode with indenting speed at 1 μ m/s was used, and the stiffness was calculated by fitting the loading portion of each

force-distance curve to the Hertzian model, assuming a Poisson's ratio of 0.4 for the samples. A total of 4-6 areas were measured in each μ RB sample, and 5 μ RB samples per group were tested.

Characterizing inter-crosslinked macroporous μ RB scaffolds using scanning electron microscopy

The morphology of inter-crosslinked gelatin μ RB scaffolds was assessed using a Hitachi S-3400N variable pressure scanning electron microscope (VP-SEM). Samples were incubated in PBS at 37 °C overnight and rinsed with DI water before being loaded to the chamber of SEM. The hydrated samples were gradually cooled from room temperature to -25 °C as the chamber pressure reduced from 1 atm to 50 Pa, following a P/T curve at which water stays liquid phase. The samples were imaged under the electron beam intensity at 15 kV and a working distance around 7 mm.

Isolation, characterization and differentiation of adipose-derived stromal cells (ASCs)

All procedures involving animals were approved by the Institutional Animal Care and Use Committee of Stanford University. Mouse ASCs were isolated from inguinal fat pads of 8-week-old, luciferase-positive transgenic mice (Jackson labs) [30]. Briefly, fat tissues were washed with HBSS and digested with Liberase enzymes (Roche Diagnostics, Indianapolis, IN) at 37°C for 1h. Then enzyme activity was neutralized with fetal bovine serum (FBS, Invitrogen, Carlsbad, CA) and cells were filtered through a 40- μ m cell strainer to remove cellular debris, and seeded into 75 cm² flasks. Following cultured at 37°C with 5% CO₂ in an incubator (Thermo Scientific, Barrington, IL, USA) for 2 days, cells were washed with PBS and expanded in Dulbecco's Modified Eagle Medium (DMEM) with fetal bovine serum (FBS, 10%), penicillin/streptomycin (100 U/ml). Cells were passaged upon 85-90% confluence and second-passage cells were used for all experiments.

ASCs were characterized by flow cytometry (FACS Arial II; BD Falcon, USA) using anti-CD73 (1:100; eBioscience, San Diego, CA, USA), anti-CD90 (1:100; eBioscience), anti-CD105 (1:100; eBioscience) and anti-CD45 (1:100; eBioscience) antibody markers, according to the manufacturer's instruction.

The in vitro differentiation capacity of the isolated ASCs was characterized. To induce osteogenic differentiation of ASCs, cells were cultured in osteogenic medium containing DMEM with FBS (10%), beta glycerol phosphate disodium salt (10 mM), dexamethasone (100 nM), L-ascorbic acid

2-phosphate (A2P, 50 $\mu\text{g}/\text{ml}$) and penicillin/streptomycin (100 U/ml). For adipogenic induction, ASCs were incubated with adipogenic medium which was comprised of DMEM, FBS (10%), penicillin/streptomycin (100 U/mL), dexamethasone (1 μM , Sigma), indomethacin (10 μM , Sigma), 3-isobutyl-1-methylxanthine (0.5 mM, Sigma), and insulin (10 $\mu\text{g}/\text{mL}$, Sigma). Medium was changed every 2-3 days. Cells were fixed with 4% paraformaldehyde and stained with alkaline phosphatase kit and Alizarin Red S (for osteogenesis) and oil red (for adipogenesis) according to the manufacturer's instructions (STEMPRO, Gibco).

Validation of injectability and in situ crosslinkability of μRB scaffolds

To test injectability of μRB s, they were rehydrated in PBS to the density of 5% (w/v), incubated at 37°C for 30 min. The rehydrated μRB s were then transferred into a 1 mL syringe, and injected through a 16 gauge needle to check if the μRB s can be ejected smoothly and homogeneously.

The in-situ crosslinking was then checked by adding 20 U/ml thrombin into the μRB s that were ejected into a custom-made cylinder mold. After incubating at 37°C for 20-30 minutes, the integrity of the formed scaffolds was examined.

To fabricate the cell-laden μRB scaffolds, the rehydrated μRB s were mixed with ASCs and injected through a 16 or 20 gauge needle into custom-made cylinder molds (50 mm³). The μRB density was varied at 5% (w/v) or 7.5% (w/v), and ASCs were encapsulated at a density of 20 million/ml. Cell/ μRB mixture were crosslinked into macroporous cell-laden scaffolds by adding 5 μl thrombin (20 U/ml). The ASC-laden μRB scaffolds were then transferred into 24-well plates for culture.

The ASC-laden μRB scaffolds without passing through injection were made as controls. Briefly, the rehydrated μRB s mixed with ASCs were sandwiched between two glass slides (with a gap of 0.5 mm), and thrombin was added subsequently to induce intercrosslinking. Samples were incubated at 37°C and for 24 h, then punched out into circular samples using biopsy puncher (3.5 mm in diameter) and transferred to 24-well plates for culture.

ASCs viability was tested by Live/Dead staining and BLI immediately after injection into 24 well plate. To test cell viability using BLI, D-luciferin (Caliper Life Sciences, Hopkinton, MA) was added to ASC-laden μRB s in 24 well plate to a final concentration of 150 $\mu\text{g}/\text{ml}$ immediately after injection. Photon counts per second were recorded using an IVIS200 (Xenogen, Alameda, CA) imaging system and analyzed with Living Image 3.2 software

(Caliper Life Sciences, Hopkinton, MA). Each well was scanned every 15 seconds until the peak signal was reached. Changes in bioluminescence intensity over time were measured and are presented as total flux values in photons/second for each well.

BMP-2 loading and release from μRB -based scaffolds

To encapsulate BMP-2 into μRB -based scaffold, 5 mg μRB s were rehydrated in 100 μl BMP-2 solution (10 $\mu\text{g}/\text{ml}$). After that, 10 μl μRB s were injected and crosslinked in situ by thrombin, resulting in 10 scaffolds with 100 ng BMP-2 loaded per scaffold.

To assess the release of BMP-2 in vitro, scaffolds containing 100 ng BMP-2 were incubated in 24 well plates with serum containing medium. At each time point, the supernatant was collected, and 1ml fresh medium was added into the well. The amount of released BMP-2 was measured by using BMP-2 ELISA kit (Peprotech, Rocky Hill, NJ).

Critical-size cranial defect surgery

Male FVB mice (7-week old, Charles River Laboratories, Hollister, CA) were used for cranial defect surgery. Briefly, mice were anesthetized with 2.5% isoflurane, and after removing the overlying pericranium, 3.3-mm cranial defects were created on the right parietal bone using a trephine drill without damaging the underlying dura mater. 10 μL of rehydrated μRB s was injected and filled into the defect, 1 μL of thrombin (200 U/mL) was added to allow in situ crosslinking. These groups are designated as "inject". To assess the effect of injection, the scaffolds fabricated using the sandwich method without passing through injection were included and designated as "implant". To assess the effect of BMP-2, the injected μRB s containing 100 ng BMP-2 per scaffold were included and designated as "inject+BMP-2". All scaffolds were made as acellular and ASC-laden groups. The mice with defect but no treatment were included as negative control, designated as "non-treated".

Bioluminescence imaging (BLI)

To evaluate cell viability after transplantation into cranial defect mice, BLI was performed in cranial defect mice that received injected or implanted ASC-laden μRB -based scaffolds from day 0 to day 14. Mice received D-luciferin (150 mg/kg) by intraperitoneal injection were placed on a heated table (37°C) with nose cone and imaged using the IVIS Spectrum system (Caliper Life Sciences, Hopkinton, MA) under 2% isoflurane anesthesia at 30-s exposure time. Each mouse was scanned every 2 minutes until the peak signal was reached. Radiance was quantified

in photons per second per centimeter squared per steradian.

X-ray microtomography

To evaluate bone regeneration of cranial defect mice, every week from week 0 to week 8, the mineralization level of the scaffolds was monitored via X-ray microtomography using a large-field Inveon PET-CT (GE, Washington, D.C.), with settings of 80 kVp X-ray voltage, 500 IA anode current, 80 μm voxel resolution, and 500 ms time for each 360 degree rotational step. The two-dimensional projection images were reconstructed into three-dimensional models with Microview (Parallax innovations Inc, Ilderton, Canada). Voxels at the supraoccipital part of the occipital bone were used as the threshold to identify mineralized bone formation. Percentage healing in each mouse was determined by calculating the percentage of reduction in the defect area using image J (NIH).

Histology and immunostaining

Calvarial of mice were harvested at day 3, week 2 and week 8 for histology. Tissues were fixed overnight at 4% paraformaldehyde, demineralized for 2 weeks in 16% ethylenediaminetetraacetic acid, and embedded in OCT for cryo-sectioning. Tissue morphology was examined by H&E staining (Sigma, St. Louis, MO, USA) and Masson trichrome staining (Thermo Scientific, Waltham, MA) according to manufacturer's instructions. For immunostaining, 20 μm sectioned slices were treated with blocking buffer consisting of 10% bovine serum albumin in 1X PBS and incubated with rat anti CD31 (BD Biosciences, San Jose, CA, USA, 1:50 dilution), rabbit anti luciferase (abcam, Cambridge, MA, USA, 1:50 dilution), mouse anti iNOS (BD Biosciences, 1:50 dilution) and mouse anti CD206 (Biolegend, San Diego, CA, USA, 1:50 dilution) overnight at 4 °C. After washing in PBS for 3 times, sectioned slices were incubated for 1 h at room temperature with secondary antibodies. Nuclei was counterstained with Hoechst 33342 stain (Thermo Scientific) and images were taken under Zeiss fluorescence microscope. Sections were stained with all reagents without primary antibody for negative controls.

Statistical analysis

All values were presented as mean \pm standard deviation. Data were analyzed by analysis of variance, followed by Turkey post hoc comparisons. Two-tailed $p < 0.05$ values were considered statistically significant. All statistical analyses were performed using GraphPad Prism (GraphPad Software, San Diego, CA).

Results and Discussion

Optimizing injectability of gelatin μRBs for forming in situ crosslinkable macroporous scaffolds

Gelatin-based μRBs were fabricated by wet-spinning as we previously reported (Figure 1A). The obtained gelatin-based μRBs were fixed using glutaraldehyde for 12 hours. According to our previous study, 12 h of glutaraldehyde incubation is required to obtain stable fixed μRB while shorter time glutaraldehyde treatment was insufficient to maintain the shape of μRB [28]. To allow the in-situ formation of the macroporous scaffolds in vivo, we introduced the thrombin catalyzed crosslinking, which has been employed for fibrin glue, an FDA-approved biomaterial with demonstrated safety and biocompatibility [31]. As compared to the previous used UV induced photo-crosslinking, this method could eliminate the potential cytotoxicity from the photo-initiator and limitation of light-penetration.

Unlike the injection of homogenous polymer precursor solution of most in-situ formation hydrogels, which can easily pass through the syringe and needles, the injection of the micron-sized μRB building blocks is subject to their stiffness and surface properties. As reported previously [28], the stiffness of individual μRB can be changed by the degree of glutaraldehyde (GTA) fixation, which was achieved by fixing μRBs in varying concentration of glutaraldehyde solution to consume different degrees of primary amines of μRBs . For example, increasing the degree of glutaraldehyde fixation from 12.5% to 37.5% led to a significant increased stiffness of μRBs , from 10 kPa to 60 kPa (Figure 1B). This increased stiffness made the μRBs more rigid and compromised the injectability. The μRBs fixed with 12.5% GTA can be injected smoothly through the syringe, but the ones fixed with 20% GTA was too rigid to be pushed through (Figure 1C). On the other hand, the fibrinogen coating which is introduced for in-situ crosslinking can also influence the injectability. Increasing fibrinogen concentration from 0.1% to 0.5% decreased the injectability. As shown in figure 1C, increasing both the degree of glutaraldehyde fixation from 12.5% to 20% and fibrinogen concentration from 0.1% to 0.5% led to phase separation (μRB phase and PBS phase) and make it unsuitable as an injectable cell carrier. This is probably due to increased stiffness and hydrophobicity of the μRBs . We found that the μRBs with 12.5% glutaraldehyde fixation and 0.1% fibrinogen coating was identified as the optimized injectable μRB formulation. The injectability allowed the μRBs to be filled into molds with different shapes (Figure 1D-F), can be in situ crosslinked by thrombin

(Figure 1E-G), and demonstrate highly interconnected macroporosity (Figure 1H-I).

Determine optimal μ RB formulation that support high cell viability post-injection

We then explored the injectability of different formulations of μ RBs encapsulated with ASCs. We found that all formulations of μ RBs supported high cell viability after encapsulation (Figure 2A). However, increasing GTA fixation from 12.5% to 20% and fibrinogen concentration from 0.1% to 0.5% led to fewer cells after injection, and the majority of cells/PBS were phase separated from μ RBs and failed to be encapsulated after injection. This is because increasing GTA concentration or fibrinogen concentration both led to increased hydrophobicity of the μ RBs, resulting in phase separation from cell/PBS mixture during injection. We identified the lead

formulation to be μ RBs fixed with 12.5% GTA, and coated with 0.1% fibrinogen, which did not cause phase separation and supported efficient cell encapsulation in μ RB hydrogel post-injection (Figure 2A). One challenge associated with injectable matrices for cell delivery is the shear force-induced cell death during the injection [32, 33]. We further determined the effects of varying μ RB density (5% or 7.5%) and needle size (16 or 20 gauge) on cell survival. ASCs cell viability was examined by live and dead staining and bioluminescent imaging. Increasing the μ RB density and decreasing the needle size can both increase the shear force sensed by the cells during injection. Indeed, we observed decreased the cell survival post-injection with higher μ RB density and smaller needle size, probably due to the high shearing force (Figure 2B-C). Importantly, ASCs maintained their osteogenic capability post-injection, as confirmed by

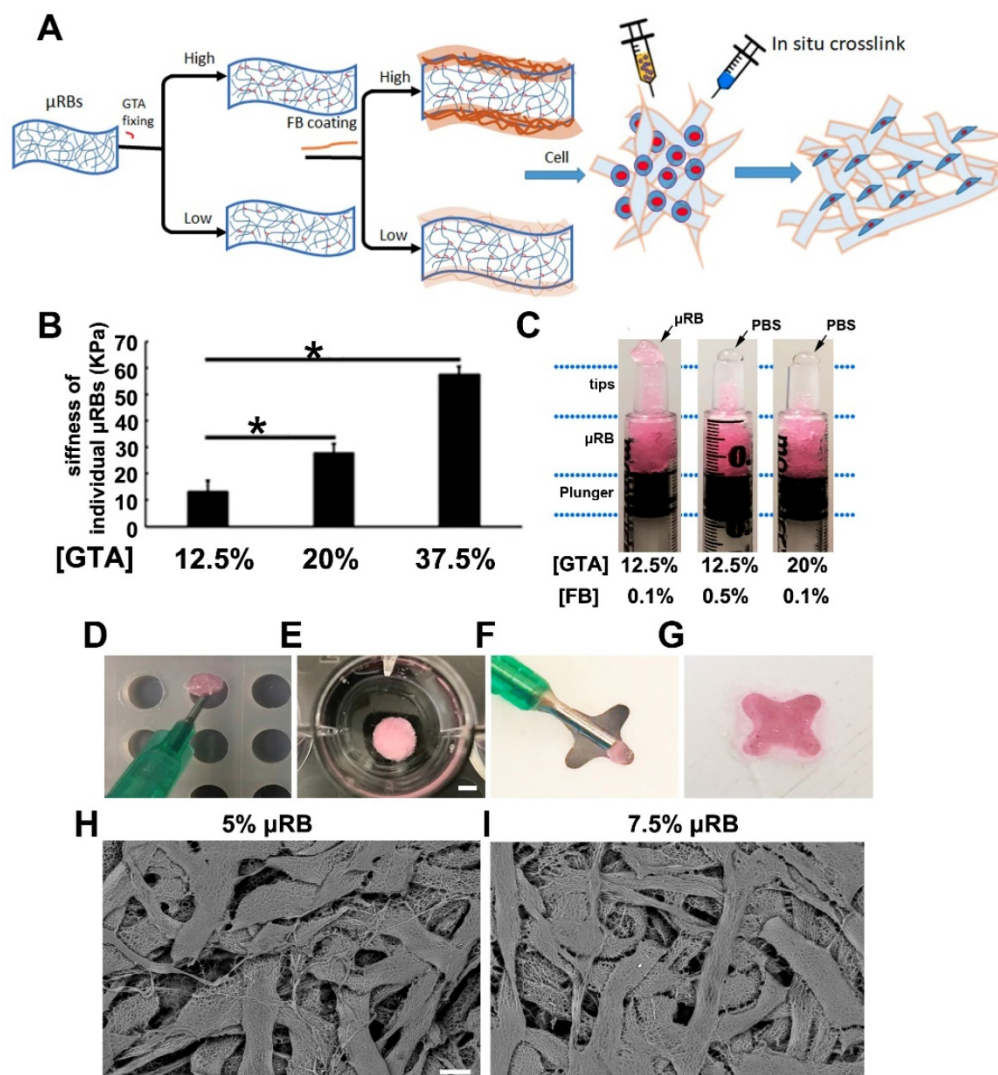


Figure 1. Fabrication and characterization of μ RB-based scaffold. (A). Gelatin-based μ RBs were firstly fabricated by wet spinning, then fixed with glutaraldehyde and coated with fibrinogen, which allow direct cell mixing and in situ crosslink with thrombin. **(B).** AFM measurement of surface stiffness of single μ RB fixed with 12.5%, 20% and 37.5% GTA. *, $p < 0.05$. **(C).** μ RBs fixed with 20% GA or 0.5% fibrinogen squeezed PBS out during injection. Injection of optimized rhodamine-labeled μ RB formulation into a cylinder mold **(D)**, scale bar=5 mm) and 4-point star mold **(F)**, crosslinked with thrombin **(E and G)**. SEM imaging of 5% **(H)**, scale bar=50 μ m) and 7.5% **(I)** μ RB-based scaffold.

ALP and ARS staining (Figure S2, Supporting Information). Based on the cell viability results, we chose 5% μ RBs fixed with 12.5% glutaraldehyde and coated with 0.1% fibrinogen as the optimal injectable formulation for the following in vivo studies. In the event where needles smaller than 16G are preferred for delivery, several strategies could be explored to further improve the cell viability after injection including decreasing the degree of GTA fixation or fibrinogen concentration, or decreasing μ RB density.

Injectable μ RB-based scaffold support cell survival in vivo, and incorporation of BMP-2 further enhances cell proliferation

Conventional injectable hydrogels are usually nanoporous, which restricts cell spreading, growth,

and tissue formation. To overcome these challenges, recent studies showed nanoporous hydrogels with dynamic cell-adaptable network can facilitate cell spreading and MSC osteogenesis. Feng et al reported a facile supramolecular gelatin hydrogels crosslinked by weak host-guest interactions that facilitate endogenous cell infiltration and migration [34]. Recently highly dynamic network of cell-infiltratable and injectable gelatin hydrogel has also been reported for promoting bone regeneration by enhancing endogenous cell infiltration [35]. The approach reported in our study is different from these previous studies in that the resulting scaffold is macroporous. Our μ RBs serve as building blocks, which can be injected through syringe and form a macroporous scaffold in situ. As such, we could combine the

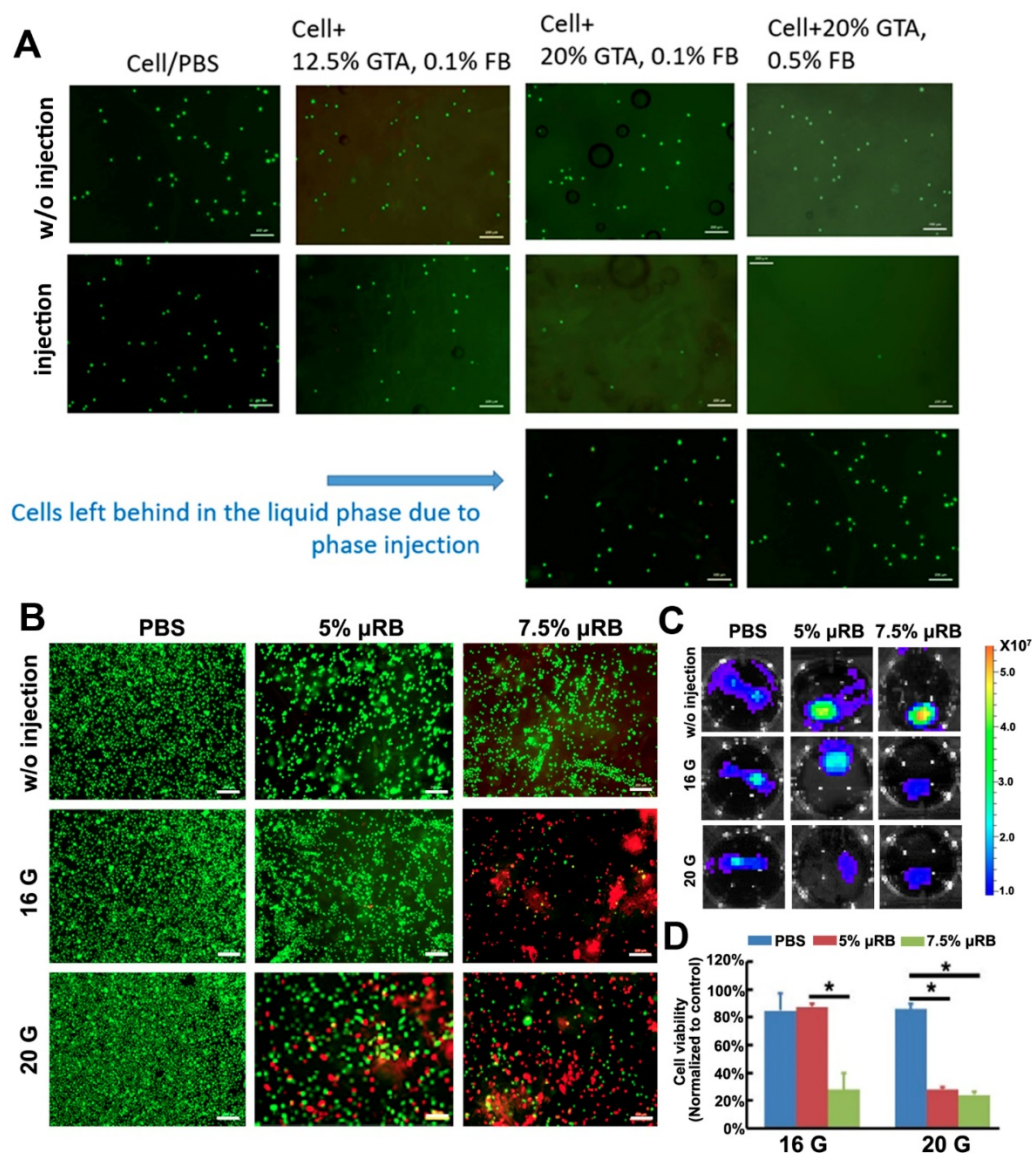


Figure 2. Optimization of injectable μ RB-based scaffold that support cell survival. (A). Live dead staining of ASC encapsulated in different formulations of μ RBs with and without injection. Green: live cells; Red: dead cells. Bar=200 μ m. (B). Live and dead imaging of ASCs that encapsulated with 5% or 7.5% μ RBs and injected through 16 gauge or 20 gauge syringe needle. Bar=200 μ m. (C). Bioluminescence imaging of ASCs that encapsulated in 5% and 7.5% μ RBs after injection through 16 gauge and 20 gauge needles. (D). Quantification data from (B). All data are presented as mean \pm S.D. *, $p < 0.05$.

injectability and macroporosity into the scaffolds for cell delivery and cell-based tissue regeneration.

By using BLI and immunohistochemical staining, we found that scaffolds supported more than 50% of ASCs survival one day after injection, and injectable μ RB group showed slightly higher cell viability even compared to the implanted prefabricated group (positive control). In addition, both injectable and implanted μ RB scaffolds supported cell proliferation, with BLI signal peaking at day 10 ($131\pm 34\%$ in injection group and $125\pm 17\%$ in implantation group vs. day 0, $p < 0.05$), highlighting the advantage of macroporosity on cell survival and proliferation. At day 10, cell number started to decline and minimum BLI signal could be detected from both groups after day 21 (Figure 3A-B). The drop of BLI signal indicates decreased number of viable cells, which may be due to nutrients competition between ASCs and infiltrated cells, such as fibroblasts and macrophages. It is also possible that increase amounts of infiltrated cells led to the formation of a dense fibrous tissue, which limits oxygen exchange and induces hypoxia, further increasing cell death [36]. Incorporation of BMP-2 in the μ RB scaffolds significantly increased cell proliferation, with a 5-fold increase of BLI signal peaking at day 7, compared to the 1.2-fold increase in the group without BMP-2 (Figure 3A-B), indicating in situ BMP-2 delivery is

beneficial for ASCs proliferation. To further confirm the cell retention and distribution, immunostaining of luciferase was performed in all the three groups. The number of transplanted ASCs (luciferase positive cells) increased from day 3 to day 7, and substantially decreased from day 7 to day 14, which was consistent with BLI data (Figure 3C).

In vivo biodegradation of μ RB scaffolds in cranial defects

To investigate biodegradation of μ RB scaffold in vivo, μ RBs were labelled with Alex flour 700 dye and injected into cranial defects. H&E staining (Figure 4A-B) and fluorescence imaging (Figure 4C-E) results showed that μ RB scaffold maintained its macroporosity for 2 weeks in vivo. A substantial decrease in scaffold size was observed at week 3, suggesting substantial degradation of the μ RB scaffolds. By week 5, minimum μ RB scaffolds could be identified from either H&E or fluorescent images. Neither addition of ASC nor BMP-2 affect the degradation of μ RB based hydrogel. Two mechanisms including hydrolysis and enzymatic degradation are responsible for gelatin-based hydrogels degradation. The main composition of gelatin after degradation contains 19 amino acids, predominantly glycine, proline and hydroxyproline. Gelatin degradation takes place in two sequential steps. In the first step,

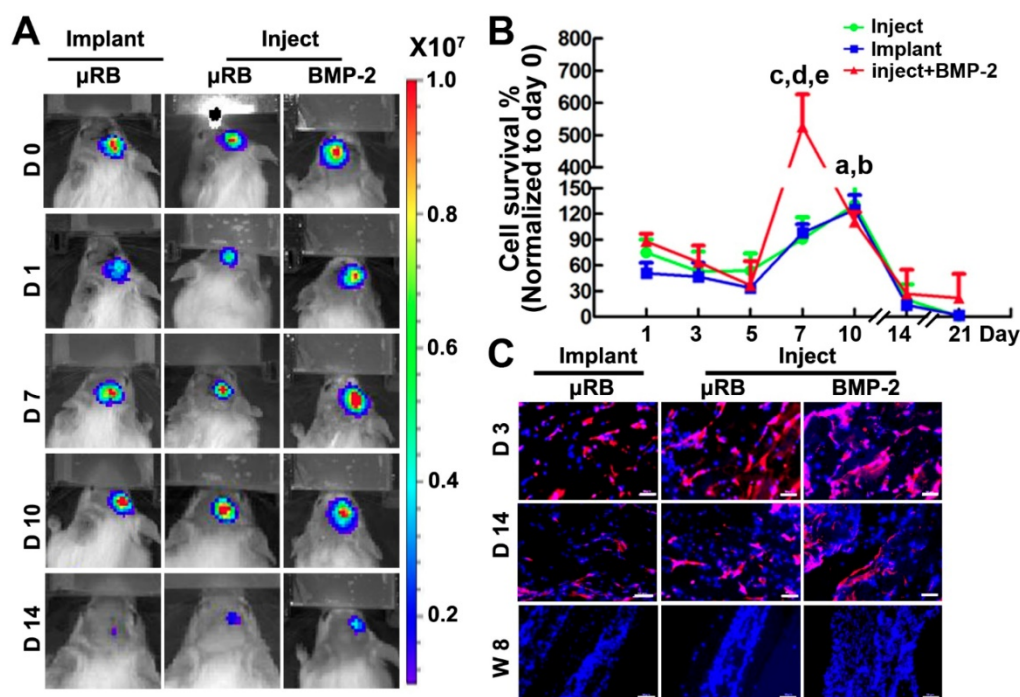


Figure 3. Cell viability after transplantation into a mouse critical size cranial defect model. (A). BLI of mice that implanted with ASC-laden μ RB scaffold or injected with ASC-laden μ RB scaffold (with and without BMP-2 incorporation) across different time points. **(B).** Quantitative data from (A). a, $p < 0.001$, Day 10 vs Day 1 in mice treated with implanted μ RBs; b, $p < 0.05$, Day 10 vs Day 1 in mice treated with injected μ RBs; c, $p < 0.001$, Day 7 vs Day 1 in mice treated with injected μ RBs+BMP-2; d, $p < 0.001$, mice treated with injected μ RBs+BMP-2 vs mice treated with injected μ RBs; e, $p < 0.001$, mice treated with injected μ RBs+BMP-2 vs mice treated with implanted μ RBs; All data are presented as mean \pm S.D. N=5 per group. **(C).** Immunostaining of luciferase in cranial defect mice implanted with ASC-laden μ RB scaffold or injected with ASC-laden μ RB scaffold (with and without BMP-2) at day 3, 7 and 14. Bar=50 μ m.

gelatinases degrade gelatin into polypeptides. Then, the polypeptides are further degraded into amino acids. Previous studies show that composition of gelatin after degradation are highly biocompatible [37]. In our study, we did not find adverse inflammatory tissue reaction *in vivo* after injection of μ RB based hydrogels (Figure 6).

Injectable gelatin μ RB-based scaffold containing BMP2 synergize with ASCs to accelerate mineralized bone formation *in vivo*

We then evaluated the efficacy of injectable gelatin μ RB scaffolds for supporting bone regeneration *in vivo* using an immunocompetent mouse critical-size cranial defect model. Mineralized bone formation was monitored for up to 8 weeks by X-ray microtomography (micro-CT). Both injectable and implantable μ RB scaffolds containing ASCs led to comparable degree of bone repair, though still slow with only ~14% bone defects filled by week 8 (Figure 5). To further accelerate mineralized bone formation, BMP-2 was directly coated onto μ RBs, and a sustained

release of BMP-2 from the μ RB scaffolds was obtained without additional modification (Fig. S3, Supporting Information). This could be due to the physical adsorption mediated through binding with fibrinogen coating [38, 39]. Bone morphogenetic proteins (BMPs) are responsible for bone formation during embryogenesis and bone regeneration and remodeling. The osteoinductive action of BMPs, especially BMP-2, has led to wide use for effective bone regeneration [40, 41]. Our results showed that BMP-2 significantly accelerated bone regeneration even without ASCs, filling up to 28%±6% bone defects by week 8. Impressively, Co-delivery of ASCs with 100 ng BMP-2 in the μ RB scaffolds exhibited great synergy, substantially accelerating bone regeneration to 86%±9% by week 8 (Figure 5A-B), Consistent with imaging, Masson's trichrome staining also demonstrated extensive collagen-rich tissue ingrowth in bone defects using injectable μ RB scaffolds containing BMP-2, and group containing both ASCs and BMP-2 leading to the most intense collagen deposition (Figure 5C). Groups without ASCs

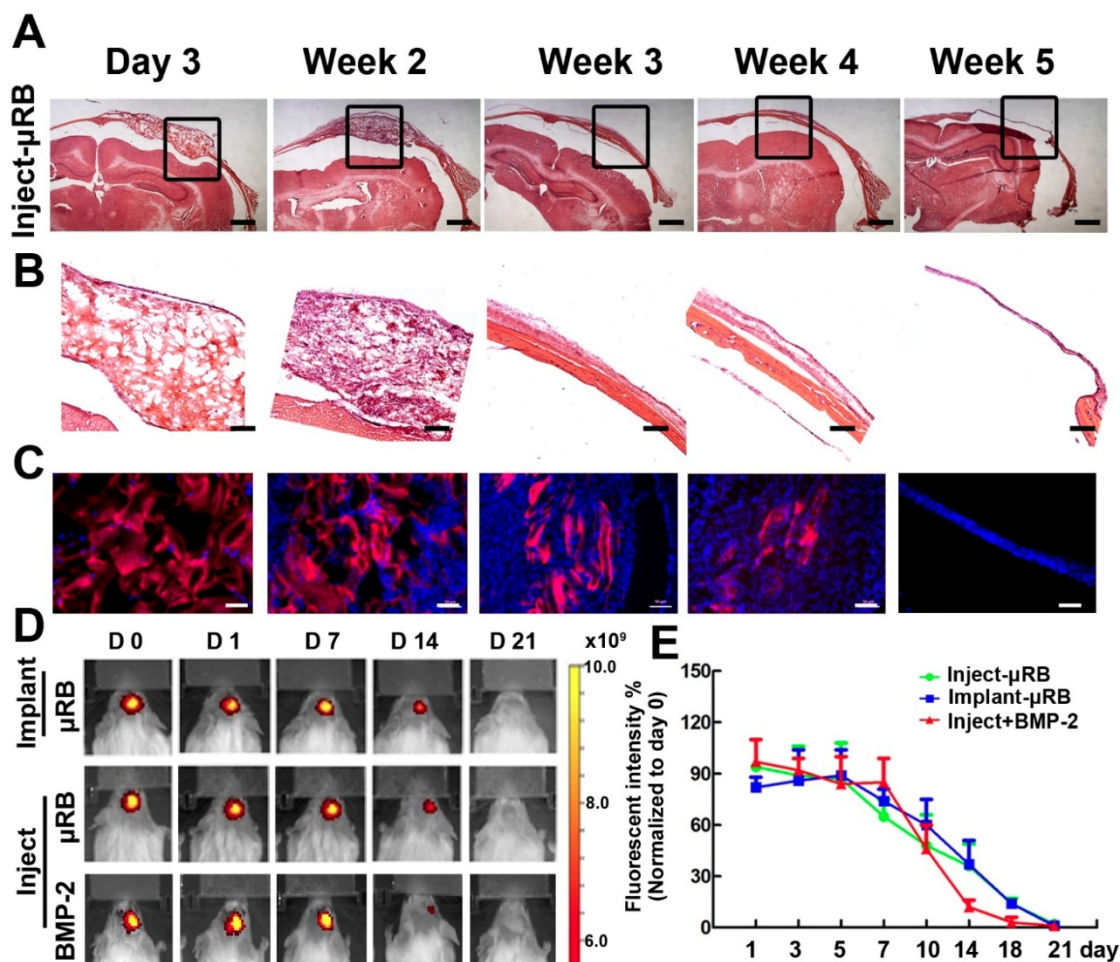


Figure 4. Degradation of μ RB-based scaffolds in a mouse critical size cranial defect model. (A). H&E staining of injected μ RB-based scaffolds harvested from cranial defect mice at day 3, week 2, week 3, week 4 and week 5. (B). High magnification of the inserts of (A). (C-D). Fluorescence imaging of injected Alex flour 700-labeled μ RB scaffolds harvested from cranial defect mice at various time points. Bar=50 μ m. (E). Quantitative data from (D). All data are presented as mean±S.D. N=5 per group.

generally showed less collagen deposition, which was more similar as non-treated control group.

Assessing inflammatory response of μ RB scaffold in vivo

Emerging evidence has highlighted the importance of inflammatory response in multiple stages of bone formation [42]. In the acute stage (0-7 days after bone defect), macrophages derived from a distinct population of blood monocytes are recruited and rapidly infiltrated into the defect area, and the majority are M1 type inflammatory macrophages [43]. In the subacute phase (7-28 days), inflammatory M1 type macrophages gradually shift to anti-inflammatory M2 type, which has been reported to be associated with bone regeneration [44, 45]. And the later chronic phase is characterized by few macrophages or giant cells.

In this study, we have specifically characterized the inflammatory response by immunostaining of

specific markers of M1 and M2 type macrophages at early (day 3), intermediate (week 2) and later stage (week 8). M1 and M2 macrophages were identified by immunofluorescent staining of M1 and M2 markers iNOS and CD206, respectively (Figure 6). Untreated cranial defect was included as a control to assess the inflammation caused by the surgery itself. The pro-inflammatory M1 type macrophages were identified in all groups at early time point (day 3), indicating acute inflammation caused by the cranial defect surgery. An inflammatory response with kinetic of macrophage population desirable for bone formation was observed in all of our experimental groups (Figure 6). Specifically, the number of inflammatory M1 macrophages dramatically decreased from day 3 to day 14 and few was detected at week 8, whereas the anti-inflammatory M2 type macrophages showed an opposite trend, with highest M2 cell number found at day 14. The shift of M1 type to M2 type is desirable for bone formation in vivo.

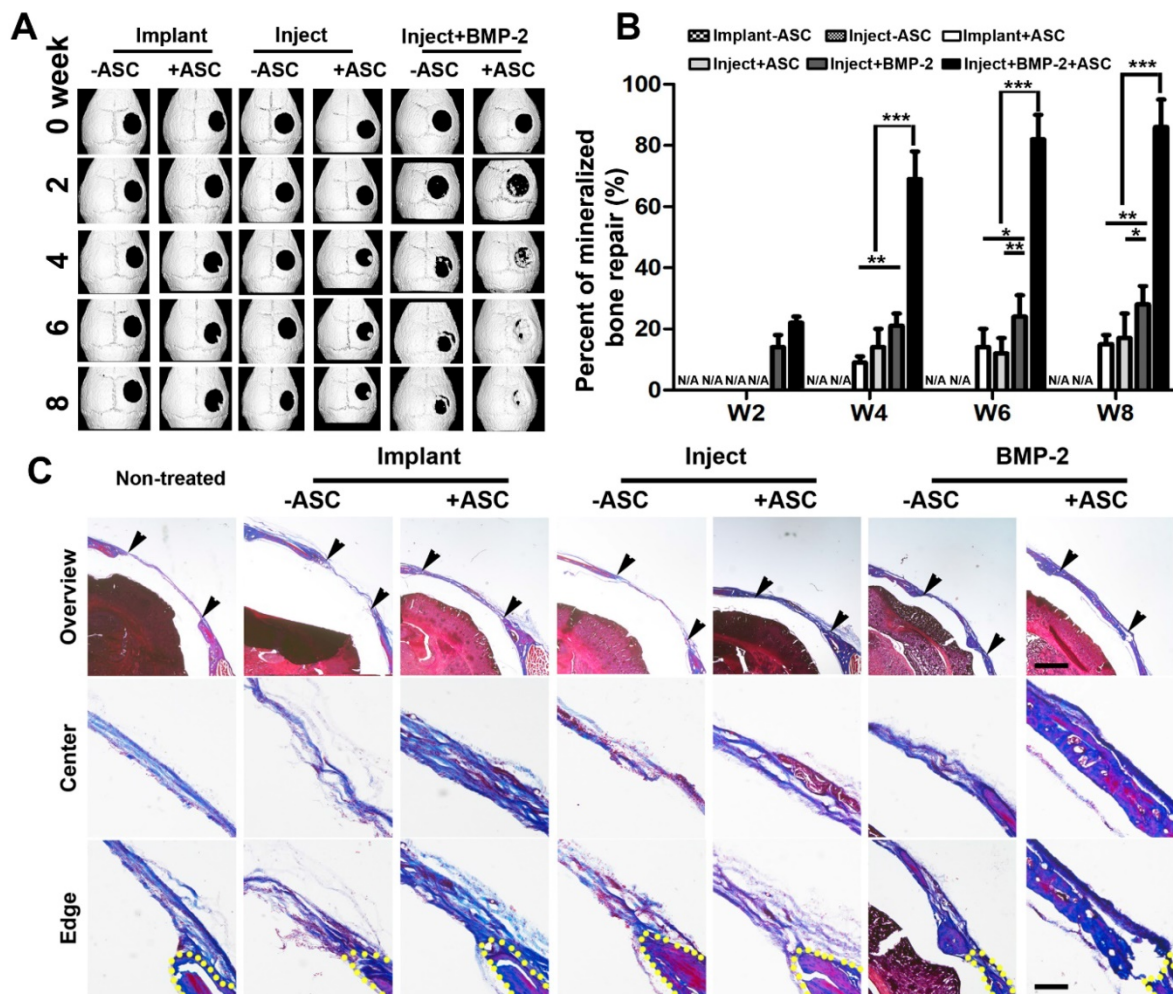


Figure 5. Micro-CT imaging of cranial defect mice across different time points and histological cross sections of mouse cranial defects at week 8. (A). Representative micro-CT images of cranial defect mice treated with injected and implanted μ RB scaffolds, and BMP-2 incorporated μ RB scaffolds, with or without ASCs. **(B).** Quantification data from (A). Percent of bone healing was normalized to the defect size at week 0. *, $p < 0.05$; **, $p < 0.01$; ***, $p < 0.001$. Data are presented as mean \pm S.D. N=5 per group. **(C).** Trichrome staining of the defect center and edge of cranial defect mice treated with injected and implanted μ RB scaffolds, and BMP-2 incorporated μ RB scaffolds, with or without ASCs, Bar=1mm (first row) and 200 μ m (middle and last row).

Importantly, groups treated with injectable or implantable gelatin μ RB scaffolds showed comparable percentage of macrophage as the untreated defect (control). In addition, we noticed that there is no significant difference of inflammatory response between cellular and acellular groups, suggesting ASCs do not affect macrophage polarization in immunocompetent mouse cranial defect model.

Vascularization of μ RB scaffold in vivo

Bone is a highly vascularized biomineralized connective tissue, and vascularization of large bone grafts is one of the main challenges of bone tissue engineering [46]. Lack of vasculature results in ineffective integration of grafts to the host vasculature upon implantation [47, 48]. Use of macroporous materials that contain interconnected channels could promote the survival of seeded cells following transplantation due to enhanced rapid nutrient diffusion [49]. We next assessed the vascularization in

the μ RB scaffolds post-transplantation in vivo, which is also critical for bone healing. Here, immunostaining of endothelial cell marker-CD31 was performed. Endothelial cell was not observed in μ RB scaffold at day 3, but emerged from day 14 and are present up to week 8 (Figure 7A), suggesting vascularization in μ RB scaffolds. Incorporation of BMP-2 significantly enhanced the vascular density, which synergize with ASCs to induce the highest degree of vascular density by week 8 (Figure 7B). This is in consistence with some previous studies, which have well documented the ability of BMP-2 for promoting angiogenesis through multiple pathways including P38, ERK and Akt/m-TOR in vitro [50, 51]. This enhanced vascularization by the BMP-2 is also correlated with the enhanced ASC proliferation (Figure 3) and bone formation in vivo (Figure 5), which could be due to the enhanced nutrient supply as a result of the vasculature.

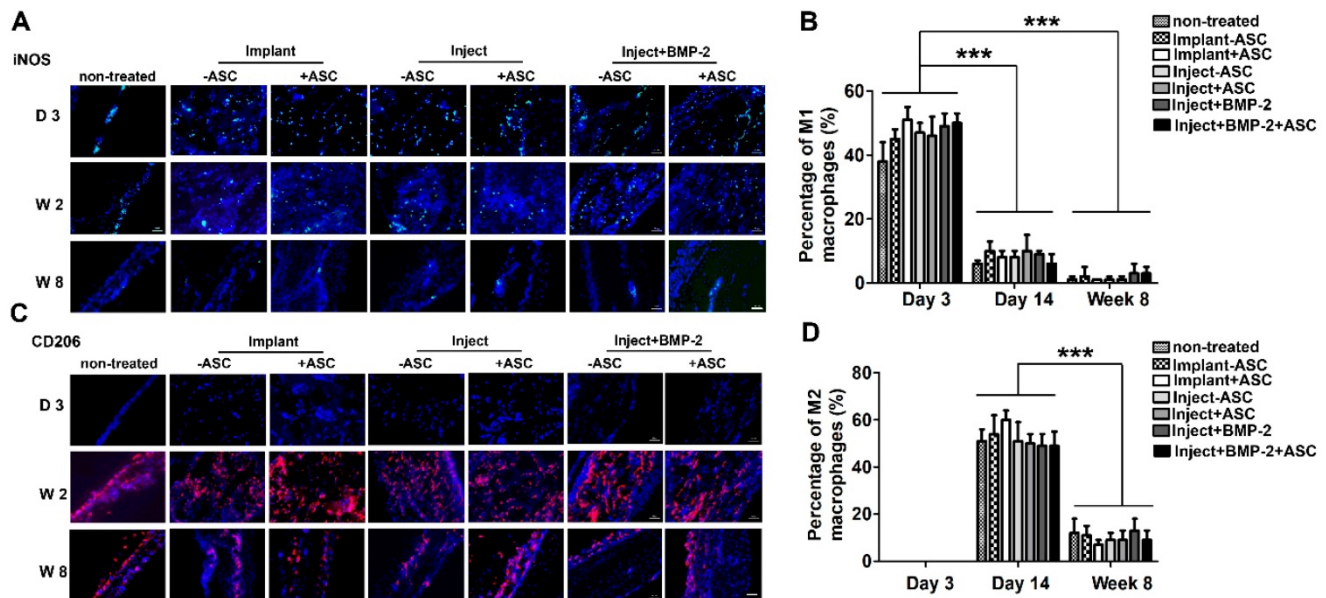


Figure 6. Inflammatory response of μ RB scaffolds in a mouse critical size cranial defect model. Immunostaining of M1 type macrophage marker iNOS (A) and M2 type of macrophage marker CD206 (C) in non-treated mice, mice transplanted with implanted ASC-laden μ RB scaffold, injected ASC-laden μ RB scaffold (with and without BMP-2 incorporation) and acellular μ RB scaffold at day 3, day 14 and week 8. (B). Quantitative data from (A). ***, $p < 0.001$. (D). Quantitative data from (C). ***, $p < 0.001$. Bar=50 μ m. All Data are presented as mean \pm S.D. N=5 per group.

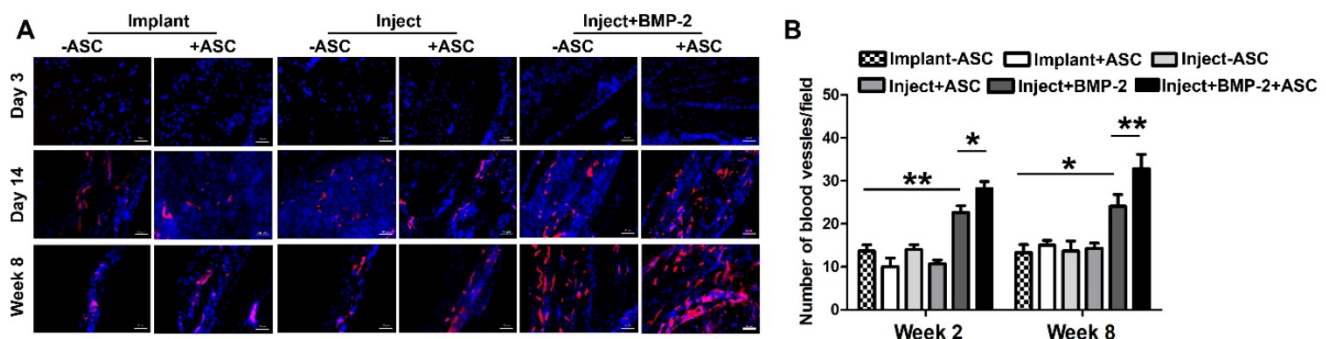


Figure 7. Vascularization in cranial defects treated with implanted and injected μ RB scaffolds. (A). Immunostaining of endothelial cell marker CD31 in cranial defect mice transplanted with implanted and injected ASC-laden μ RB (with and without BMP-2) scaffold and acellular μ RB-based scaffold at day 3, 14 and week 8. Red=CD31, Blue=DAPI. Bar=50 μ m. (B). Quantitative data from (A). *, $p < 0.05$; **, $p < 0.01$. All Data are presented as mean \pm S.D. N=5 per group.

Conclusion

In summary, here we fabricated a gelatin-based μ RB scaffolds for cell delivery, which is specifically optimized to be injectable and in situ crosslinkable. The μ RBs are crosslinked by fibrinogen mediated by a blood clotting mechanism, which is biocompatible and widely used in fibrin glue as bio-adhesives. The injectability of the μ RBs was optimized by adjusting the degree of glutaraldehyde fixation, fibrinogen coating, μ RB density and syringe needle size. The optimized μ RBs well supported cell survival and proliferation in vivo post-injection. Using an immunocompetent mouse critical-size cranial defect model, we further demonstrated that injected μ RB-based scaffold supported ASC based bone formation in vivo, which performed comparably to implanted μ RB-based scaffold. In addition, the μ RBs can be used for co-delivery of BMP-2 with ASCs, which synergistically enhanced bone regeneration in vivo and enhanced vascularization. Our injectable μ RB-based scaffold allows easy delivery of stem cells and growth factors into the defect area in a minimal invasive manner, and can be broadly used as injectable macroporous matrices to deliver various cell types for tissue regeneration.

Abbreviations

ASC: adipose-derived stromal cell; ALP: alkaline phosphatase; ARS: alizarin red; BMP-2: Bone morphogenetic protein 2; μ RB: microribbon.

Supplementary Material

Supplementary figures and tables.

<http://www.thno.org/v10p6035s1.pdf>

Acknowledgements

The authors would like to thank NIH R01DE024772, California Institute for Regenerative Medicine (Grant #RT3-07804), National Science Foundation CAREER award program (CBET-1351289), and Stanford Chem-H Institute for funding.

Competing Interests

The authors have declared that no competing interest exists.

References

- Parisi-Amon A, Mulyasmita W, Chung C, Heilshorn SC. Protein-engineered injectable hydrogel to improve retention of transplanted adipose-derived stem cells. *Adv Healthc Mater.* 2013; 2: 428-32.
- Samper E, Diez-Juan A, Montero JA, Sepulveda P. Cardiac cell therapy: boosting mesenchymal stem cells effects. *Stem Cell Rev Rep.* 2013; 9: 266-80.
- Terrovitis JV, Smith RR, Marban E. Assessment and optimization of cell engraftment after transplantation into the heart. *Circ Res.* 2010; 106: 479-94.
- Hidalgo-Bastida LA, Cartmell SH. Mesenchymal stem cells, osteoblasts and extracellular matrix proteins: enhancing cell adhesion and differentiation for bone tissue engineering. *Tissue Eng Part B Rev.* 2010; 16: 405-12.
- Mitrousis N, Fokina A, Shoichet MS. Biomaterials for cell transplantation. *Nat Rev Mater.* 2018; 3: 441-56.
- Dong Y, Rodrigues M, Li X, Kwon SH, Kosaric N, Khong S, et al. Injectable and tunable gelatin hydrogels enhance stem cell retention and improve cutaneous wound healing. *Adv Funct Mater.* 2017; 27: 1606619.
- Ji X, Yuan X, Ma L, Bi B, Zhu H, Lei Z, et al. Mesenchymal stem cell-loaded thermosensitive hydroxypropyl chitin hydrogel combined with a three-dimensional-printed poly(ϵ -caprolactone) /nano-hydroxyapatite scaffold to repair bone defects via osteogenesis, angiogenesis and immunomodulation. *Theranostics.* 2020; 10: 725-40.
- Jabbari E. Hydrogels for Cell Delivery. *Gels.* 2018; 4.
- Zhao X, Liu S, Yildirim L, Zhao H, Ding R, Wang H, et al. Injectable stem cell - laden photocrosslinkable microspheres fabricated using microfluidics for rapid generation of osteogenic tissue constructs. *Adv Funct Mater.* 2016; 26: 2809-19.
- Li J, Mooney DJ. Designing hydrogels for controlled drug delivery. *Nat Rev Mater.* 2016; 1.
- Lu P, Takai K, Weaver VM, Werb Z. Extracellular matrix degradation and remodeling in development and disease. *Cold Spring Harb Perspect Biol.* 2011; 3.
- Loh QL, Choong C. Three-dimensional scaffolds for tissue engineering applications: role of porosity and pore size. *Tissue Eng Part B Rev.* 2013; 19: 485-502.
- Bencherif SA, Braschler TM, Renaud P. Advances in the design of macroporous polymer scaffolds for potential applications in dentistry. *J Periodontol Implant Sci.* 2013; 43: 251-61.
- Qutachi O, Vetsch JR, Gill D, Cox H, Scurr DJ, Hofmann S, et al. Injectable and porous PLGA microspheres that form highly porous scaffolds at body temperature. *Acta Biomater.* 2014; 10: 5090-8.
- Park SH, Gil ES, Kim HJ, Lee K, Kaplan DL. Relationships between degradability of silk scaffolds and osteogenesis. *Biomaterials.* 2010; 31: 6162-72.
- Dawson JL, Wahl DA, Lanham SA, Kanczler JM, Czernuszka JT, Oreffo RO. Development of specific collagen scaffolds to support the osteogenic and chondrogenic differentiation of human bone marrow stromal cells. *Biomaterials.* 2008; 29: 3105-16.
- Nam YS, Yoon JJ, Park TG. A novel fabrication method of macroporous biodegradable polymer scaffolds using gas foaming salt as a porogen additive. *J Biomed Mater Res.* 2000; 53: 1-7.
- Barry RA, Shepherd RF, Hanson JN, Nuzzo RG, Wiltzius P, Lewis JA. Direct-Write Assembly of 3D Hydrogel Scaffolds for Guided Cell Growth. *Adv Mater.* 2009; 21: 2407-10.
- DeVolder RJ, Bae H, Lee J, Kong H. Directed blood vessel growth using an angiogenic microfiber/microparticle composite patch. *Adv Mater.* 2011; 23: 3139-43.
- Tarafder S, Balla VK, Davies NM, Bandyopadhyay A, Bose S. Microwave-sintered 3D printed tricalcium phosphate scaffolds for bone tissue engineering. *J Tissue Eng Regen Med.* 2013; 7: 631-41.
- Ooi A, Song DH. Reducing infection risk in implant-based breast-reconstruction surgery: challenges and solutions. *Breast Cancer (Dove Med Press).* 2016; 8: 161-72.
- Bose S, Roy M, Bandyopadhyay A. Recent advances in bone tissue engineering scaffolds. *Trends Biotechnol.* 2012; 30: 546-54.
- Bencherif SA, Sands RW, Bhatta D, Arany P, Verbeke CS, Edwards DA, et al. Injectable preformed scaffolds with shape-memory properties. *Proc Natl Acad Sci U S A.* 2012; 109: 19590-5.
- Koshy ST, Ferrante TC, Lewin SA, Mooney DJ. Injectable, porous, and cell-responsive gelatin cryogels. *Biomaterials.* 2014; 35: 2477-87.
- Bencherif SA, Warren Sands R, Ali OA, Li WA, Lewin SA, Braschler TM, et al. Injectable cryogel-based whole-cell cancer vaccines. *Nat Commun.* 2015; 6: 7556.
- Griffin DR, Weaver WM, Scumpia PO, Di Carlo D, Segura T. Accelerated wound healing by injectable microporous gel scaffolds assembled from annealed building blocks. *Nat Mater.* 2015; 14: 737-44.
- Caldwell AS, Campbell GT, Shekiro KMT, Anseth KS. Clickable Microgel Scaffolds as Platforms for 3D Cell Encapsulation. *Adv Healthc Mater.* 2017; 6.
- Han LH, Yu S, Wang T, Behn AW, Yang F. Microribbon - Like Elastomers for Fabricating Macroporous and Highly Flexible Scaffolds that Support Cell Proliferation in 3D. *Adv Funct Mater.* 2013; 23: 346-58.
- Han LH, Tong X, Yang F. Photo-crosslinkable PEG-based microribbons for forming 3D macroporous scaffolds with decoupled niche properties. *Adv Mater.* 2014; 26: 1757-62.
- Han LH, Conrad B, Chung MT, Deveza L, Jiang X, Wang A, et al. Winner of the Young Investigator Award of the Society for Biomaterials at the 10th World Biomaterials Congress, May 17-22, 2016, Montreal QC, Canada: Microribbon-based hydrogels accelerate stem cell-based bone regeneration in a mouse critical-size cranial defect model. *J Biomed Mater Res A.* 2016; 104: 1321-31.
- Lutolf MP, Hubbell JA. Synthetic biomaterials as instructive extracellular microenvironments for morphogenesis in tissue engineering. *Nat Biotechnol.* 2005; 23: 47-55.

32. Aguado BA, Mulyasmita W, Su J, Lampe KJ, Heilshorn SC. Improving viability of stem cells during syringe needle flow through the design of hydrogel cell carriers. *Tissue Eng Part A*. 2012; 18: 806-15.
33. Tong X, Yang F. Recent Progress in Developing Injectable Matrices for Enhancing Cell Delivery and Tissue Regeneration. *Adv Healthc Mater*. 2018; 7: e1701065.
34. Feng Q, Wei K, Lin S, Xu Z, Sun Y, Shi P, et al. Mechanically resilient, injectable, and bioadhesive supramolecular gelatin hydrogels crosslinked by weak host-guest interactions assist cell infiltration and in situ tissue regeneration. *Biomaterials*. 2016; 101: 217-28.
35. Feng Q, Xu J, Zhang K, Yao H, Zheng N, Zheng L, et al. Dynamic and Cell-Infiltratable Hydrogels as Injectable Carrier of Therapeutic Cells and Drugs for Treating Challenging Bone Defects. *ACS Cent Sci*. 2019; 5: 440-50.
36. Baker BM, Gee AO, Metter RB, Nathan AS, Marklein RA, Burdick JA, et al. The potential to improve cell infiltration in composite fiber-aligned electrospun scaffolds by the selective removal of sacrificial fibers. *Biomaterials*. 2008; 29: 2348-58.
37. Ullm S, Kruger A, Tondera C, Gebauer TP, Neffe AT, Lendlein A, et al. Biocompatibility and inflammatory response in vitro and in vivo to gelatin-based biomaterials with tailorable elastic properties. *Biomaterials*. 2014; 35: 9755-66.
38. Morgan AW, Chan LL, Sendemir-Urkmez A, Cunningham BT, Jamison RD. Detection of growth factor binding to gelatin and heparin using a photonic crystal optical biosensor. *Mater Sci Eng C*. 2010; 30: 686-90.
39. Martino MM, Briquez PS, Ranga A, Lutolf MP, Hubbell JA. Heparin-binding domain of fibrin(ogen) binds growth factors and promotes tissue repair when incorporated within a synthetic matrix. *Proc Natl Acad Sci U S A*. 2013; 110: 4563-8.
40. Sheikh Z, Javaid MA, Hamdan N, Hashmi R. Bone Regeneration Using Bone Morphogenetic Proteins and Various Biomaterial Carriers. *Materials (Basel)*. 2015; 8: 1778-816.
41. Zhang W, Zhu C, Wu Y, Ye D, Wang S, Zou D, et al. VEGF and BMP-2 promote bone regeneration by facilitating bone marrow stem cell homing and differentiation. *Eur Cell Mater*. 2014; 27: 1-11; discussion -2.
42. Lorenzo J, Horowitz M, Choi Y. Osteoimmunology: interactions of the bone and immune system. *Endocr Rev*. 2008; 29: 403-40.
43. Gu Q, Yang H, Shi Q. Macrophages and bone inflammation. *J Orthop Translat*. 2017; 10: 86-93.
44. Gibon E, Loi F, Cordova LA, Pajarinen J, Lin T, Lu L, et al. Aging Affects Bone Marrow Macrophage Polarization: Relevance to Bone Healing. *Regen Eng Transl Med*. 2016; 2: 98-104.
45. Jablonski KA, Amici SA, Webb LM, Ruiz-Rosado Jde D, Popovich PG, Partida-Sanchez S, et al. Novel Markers to Delineate Murine M1 and M2 Macrophages. *PLoS One*. 2015; 10: e0145342.
46. Mercado-Pagan AE, Stahl AM, Shanjani Y, Yang Y. Vascularization in bone tissue engineering constructs. *Ann Biomed Eng*. 2015; 43: 718-29.
47. Fan C, Wang DA. Macroporous Hydrogel Scaffolds for Three-Dimensional Cell Culture and Tissue Engineering. *Tissue Eng Part B Rev*. 2017; 23: 451-61.
48. Xiao X, Wang W, Liu D, Zhang H, Gao P, Geng L, et al. The promotion of angiogenesis induced by three-dimensional porous beta-tricalcium phosphate scaffold with different interconnection sizes via activation of PI3K/Akt pathways. *Sci Rep*. 2015; 5: 9409.
49. Annabi N, Nichol JW, Zhong X, Ji C, Koshy S, Khademhosseini A, et al. Controlling the porosity and microarchitecture of hydrogels for tissue engineering. *Tissue Eng Part B Rev*. 2010; 16: 371-83.
50. Zuo WH, Zeng P, Chen X, Lu YJ, Li A, Wu JB. Promotive effects of bone morphogenetic protein 2 on angiogenesis in hepatocarcinoma via multiple signal pathways. *Sci Rep*. 2016; 6: 37499.
51. Luo C, Fang H, Zhou M, Li J, Zhang X, Liu S, et al. Biomimetic open porous structured core-shell microtissue with enhanced mechanical properties for bottom-up bone tissue engineering. *Theranostics*. 2019; 9: 4663-77.